

Supporting Information for

Effects of Bi and Sb ion incorporation on the optoelectronic properties of mixed lead-tin perovskites

F. M. Rombach,^a L. Gregori,^b A. Sidler,^c J. Whitworth,^d S. Zeiske,^{e,f} H. Jin,^a E. Hung,^a S. Motti,^g P.

Caprioglio,^a A. Ardalan,^c M. Lenz,^c D. Meggiolaro,^{h,*} F. De Angelis,^{b,h,i} H. J. Snaith^{a,*}

^a*Department of Physics, University of Oxford, Clarendon Laboratory, Parks Road, Oxford, OX1 3PU, UK*

^b*Department of Chemistry, Biology and Biotechnology, University of Perugia, Via Elce di Sotto 8, 06123, Perugia, Italy.*

^c*Institute for Ecopreneurship, School of Life Sciences, University of Applied Sciences and Arts Northwestern Switzerland, Hofackerstrasse 30, 4132 Muttenz, Switzerland*

^d*Materials Innovation Factory, University of Liverpool, 51 Oxford Street, Liverpool L7 3NY, UK*

^e*Sustainable Advanced Materials (Sêr-SAM), Centre for Integrative Semiconductor Materials and Department of Physics, Swansea University Bay Campus, Fabian Way, Swansea, SA1 8EN, UK*

^f*Department of Chemistry, Northwestern University, 2145 Sheridan Rd, Evanston, IL 60208, USA*

^g*School of Physics and Astronomy, Faculty of Engineering and Physical Sciences, University of Southampton, University Road, Southampton SO17 1BJ, UK*

^h*Computational Laboratory for Hybrid/Organic Photovoltaics (CLHYO), Istituto CNR di Scienze e Tecnologie Chimiche (SCITEC-CNR), Via Elce di Sotto 8, 06123, Perugia, Italy.*

ⁱ*SKKU Institute of Energy Science and Technology (SIEST) Sungkyunkwan University, Suwon, Korea 440-746.*

Email: daniele.meggiolaro@cnr.it, henry.snaith@physics.ox.ac.uk

Experimental Methods

Preparation of perovskite precursors

To make a 1.8M $\text{FA}_{0.83}\text{Cs}_{0.17}\text{Pb}_{0.5}\text{Sn}_{0.5}\text{I}_3$ perovskite precursor, FAI (1.49 mmol, Greatcellsolar), CsI (0.31 mmol, Alfa Aesar, 99.9%), PbI_2 (0.90 mmol, Thermo Fisher Scientific, ultra dry 99.999%), SnI_2 (0.90 mmol, Thermo Fisher Scientific, ultra dry 99.999%), SnF_2 (0.09 mmol, Aldrich, 99%), and metallic Sn powder (10 mg, Aldrich, 99.5%) were stirred in DMF (0.800 ml, Sigma Aldrich, anhydrous) and DMSO (0.200 ml, Sigma Aldrich, anhydrous) for 4 days at room temperature in a glovebox. BiI_3 (Thermo Fisher Scientific, Puratronic, 99.999%) and SbI_3 (Thermo Fisher Scientific, ultra dry 99.998%) dopants were dissolved in 4:1 DMSO:DMF to make stock solutions, which were added to the perovskite precursor 60 minutes before spincoating. The undoped control precursor was appropriately diluted with an equal volume of DMF:DMSO to ensure concentrations of all precursor inks remained the same. For small concentrations of BiI_3 and SbI_3 doping, successive dilutions of doped precursor ink with undoped precursor ink were carried out. Solutions were filtered with a 0.45 μm PTFE filter shortly before spincoating.

Perovskite film fabrication

Glass or indium tin oxide (ITO) substrates (Biotain, 10-15 Ω/cm^2) were cleaned by scrubbing with dishwashing soap, then sonicated for 10 min in 1 vol% Decon90 in DI water. Substrates were then rinsed with DI water and sonicated in DI water for 10 minutes, then sonicated in acetone and IPA for 5 minutes each. Substrates were dried with N_2 and exposed to UV ozone for 10 minutes immediately before further processing. Al_2O_3 NPs were added to the substrate to improve wetting. 90 μl of a Al_2O_3 nanoparticle suspension (Sigma Aldrich, <50 nm, 20%wt in IPA, diluted 1:150 in IPA) was deposited on the substrate by dynamic dropping during spinning at 5000 rpm for 30 seconds and subsequently dried for 2 minutes at 100°C. To deposit perovskite films, 80 μl of the perovskite precursor was statically dropped and spread onto the substrate, then spun at 5000 rpm and 1000 acc for 60 seconds. 200 μl of anisole (anhydrous, Sigma-Aldrich) antisolvent was dropped onto the substrate after 30 seconds. The substrates were then annealed at 100°C for 15 minutes. Samples were encapsulated with

a glass slide attached to the substrate with UV-activated epoxy which was cured for 3 minutes (Everlight Eversolar AB-341). A recessed cavity glass with epoxy only deposited at the encapsulation edge was used to allow for optical measurements. Before encapsulation, perovskite material was removed at the epoxy edge for optimal adhesion.

Photoluminescence Quantum Efficiency

Photoluminescence quantum efficiency (PLQE) of samples was determined according to the method of de Mello et al.¹ Samples were placed inside an integrating sphere and excited from the substrate side with a 657 nm continuous wave laser excitation source (Thorlabs) at 70.9 mW cm^{-2} (equivalent to one sun for a 1.25 eV bandgap) with a large spot size of 0.15 cm^2 . The resulting PL signal was collected via a fibre bundle (Ocean Optics QR600 7 SR125BX) coupled with a spectrometer (QE Pro, Ocean Optics). Two different spots were measured on each substrate.

We applied a stray light correction to recorded PL spectra by subtracting the spectrum of the excitation laser (attenuated to the correct intensity according to the fraction of laser absorbed by the sample). Photoluminescence emission spectra with a signal-to-noise ratio below 2 were not used, which corresponded to a noise floor of 0.03% PLQE at a 1 sun illumination intensity. Additionally, the detector used was not able to effectively detect PL above 1050 nm, which means that for the 1.25 eV bandgap samples used here, we were only able to map slightly more than half of the PL emission peak. To correct this, we fit the PL measurements to a Pseudo-Voigt function and used the resulting peaks to calculate PLQE (fits were only used if $R^2 > 0.8$ was achieved).

Time-resolved Photoluminescence

Time-resolved photoluminescence (TRPL) measurements were collected by exciting samples from the substrate side with a 630 nm laser head (LDH-635, PicoQuant GmbH) pulsed at a frequency of

10 kHz with a fluence of $3.1 \text{ nJ cm}^{-2} \text{ pulse}^{-2}$ and a spot size of $2.4 \times 10^{-3} \text{ cm}^2$. The time-resolved PL signal was collected from the same side with a time-correlated single photon counting (TCSPC) setup (FluoTime 300, PicoQuant GmbH using a TimeHarp260 for photon counting). The emission was individually attenuated to keep the detector pile-up rate under 5%.

The resulting data was normalized, and the tails of the resulting decays ($>200 \text{ ns}$) were fit with a stretched mono-exponential decay. Fits were performed from 200 ns until the point in the decay where the signal-to-noise ratio fell below 2. For decays with lifetimes shorter than 200 ns, fits were performed on the 50 ns before the point in the decay where the signal-to-noise ratio fell below 2.

X-ray Diffraction

X-ray diffraction (XRD) measurements were performed on a Panalytical X'pert Pro XRD diffractometer using a Cu-k(alpha) radiation source with a wavelength of 1.54 eV and a generator voltage of 40 V and current of 40 mA. To track any effects related to oxidation during measurements, we perform several successive scans on each sample. During the 2.5-hour measurement duration we didn't observe formation of additional peaks and observed only a very slight ($< 0.1^\circ$) peak shift of the perovskite phase to lower angles.

UV-vis-NIR absorbance

The total transmittance and total reflectance of encapsulated samples were measured in a Cary 5000 spectrophotometer using an internal diffuse reflectance accessory. Absorbance was calculated according to $A = -\ln_{10}(1 - T - R)$.

Ultra-sensitive External Quantum Efficiency

Ultra-sensitive external quantum efficiency (EQE) measurements were conducted on non-encapsulated perovskite films on glass with various densities of Bi³⁺ doping. To enable electrical measurements, gold photoresistor electrodes were evaporated on top. A spectrophotometer (Perkin Elmer, Lambda 950) was used as a light source. The probe light was physically chopped at 273 Hz (Thorlabs MC2000B) and guided on the device under test (DUT) using different optical components. Prior analyzing the DUT response with a lock-in amplifier, the photocurrent was fedged through a current pre-amplifier with variable gain and low-noise voltage source (Femto, DLPCA-200). Details to the EQE setup are provided elsewhere.² The DUTs were mounted in an electrically shielded (Faraday cage-like) sample holder from Linkam; the DUTs in the sample holder were kept under dry nitrogen-circulation. EQE measurements were conducted at -10 V applied bias voltage using the Femto current pre-amplifier; an electrical bandwidth of 1 mHz was used. Furthermore, a 975 nm optical density (OD) 4.0 longpass filter was placed into the light path for low-photon energy (i.e., at photon energies well below the bandgap) measurements to further reduce the (optical) noise.

Computational Details

DFT calculations have been conducted in the 2x2x2 supercell of the tetragonal MAPb_{0.5}Sn_{0.5}I₃ phase by using the Quantum Espresso software package.³ The equilibrium structure of defects have been found by relaxing the lattice by using the Perdew-Burke-Ernzherof (PBE) functional and by including DFT-D3 dispersion corrections,⁴ keeping cell parameters fixed to the experimental values.⁵ DFT calculations in supercells have been carried out at the Γ point in the Brillouin zone (BZ) by using norm-conserving pseudopotentials^{6,7} with a cutoff on the wavefunctions of 60 Ry. Defect quantities have been refined by using the PBE0 functional^{9,10} with a decreased fraction of exact exchange $\alpha = 0.20$, by including spin-orbit corrections (SOC) and DFT-D3 dispersions. By using the PBE0 functional ($\alpha = 0.20$) and including SOC a band gap of 1.29 eV has been obtained for the MAPb_{0.5}Sn_{0.5}I₃ phase, nicely matching the experimental value. Hybrid-SOC calculations have been

conducted by using the same methodology employed for PBE calculations, by reducing exact exchange cutoff to 60 Ry to reduce the computational effort.

Defect formation energies (DFE) and thermodynamic ionization levels ε have been calculated according to the following equations:⁸

$$DFE [X^q] = E[X^q] - E[perf] - \sum_i n_i \mu_i + q(\varepsilon_{VB} + \varepsilon_F) + E_{corr}^q \quad (1)$$

$$\varepsilon(q/q') = \frac{E[X^q] - E[X^{q'}]}{q' - q} + \frac{E_{corr}^q - E_{corr}^{q'}}{q' - q} - \varepsilon_{VB} \quad (2)$$

where $E(X^q)$ is the energy of the supercell containing defect X, $E(perf)$ is the energy of the non-defective system, n and μ are, respectively, the number and the chemical potentials of the species added or subtracted to the non-defective system to form a defect; q is the charge of the defect. Long-range electrostatic interactions E_{corr}^q have been corrected through the Makov-Payne scheme by using the ionic dielectric permittivity of MAPbI₃ ($\varepsilon=25$).

The chemical potentials of the atomic species have been set in order to simulate I-rich, I-medium, and I-poor conditions of growth, under the constraint of the thermodynamic stability of the MAPb_{0.5}Sn_{0.5}I₃ phase. In I-rich conditions the following values of the chemical potentials have been used $\mu(I) = (\mu(SnI_4) - \mu(SnI_2))/2 = -0.17$ eV vs I_2^{solid} ; $\mu(Sn) = \mu(SnI_2) - 2\mu(I) = -1.40$ eV vs $\mu(Sn_{bulk})$; $\mu(Pb) = \mu(PbI_2) - 2\mu(I) = -1.58$ eV vs $\mu(Pb_{bulk})$. In I-poor conditions $\mu(I) = (\mu(SnI_2) - \mu(Sn_{bulk}))/2 = -0.87$ eV vs I_2^{solid} ; $\mu(Sn) = \mu(Sn_{bulk}) = 0.0$ eV vs $\mu(Sn_{bulk})$; $\mu(Pb) = \mu(PbI_2) - 2\mu(I) = -0.18$ eV vs $\mu(Pb_{bulk})$. For I-medium conditions intermediate chemical potentials between I-rich and I-poor have been used. The chemical potentials of the Bi and Sb dopants have been calculated by considering the stability limit of the respective trivalent Bi/SbI₃ salts, i.e. $\mu(Bi/Sb) = \mu(Bi/SbI_3) - 3\mu(I)$. The energy of the phases have been evaluated at the experimental crystal structures.¹¹

TRPL and PLQE simulations

The change in carrier density in space and over time was simulated using the equations below. The processes of 1D diffusion, Auger recombination, bimolecular radiative recombination, and trap-assisted non-radiative recombination were simulated. The equations below show recombination with one electron trap as an example – simulations were performed with up to three traps, with a separate ODE for each trap occupancy. Calculation of the various parameters and recombination rates was performed via equations 6-13.

$$\frac{dn}{dt}(x, t) = G(x, t) - D_n \frac{d^2n}{dx^2}(x, t) - R_{aug}(x, t) - R_{rad}(x, t) - R_{trap\ 1,n}(x, t) \quad (3)$$

$$\frac{dp}{dt}(x, t) = G(x, t) - D_p \frac{d^2p}{dx^2}(x, t) - R_{aug}(x, t) - R_{rad}(x, t) - R_{trap\ 1,p}(x, t) \quad (4)$$

$$\frac{dn_{trap\ 1}}{dt}(x, t) = R_{trap\ 1,n}(x, t) - R_{trap\ 1,p}(x, t) \quad (5)$$

Parameter	Symbol	Units	Value
Charge carrier density (electron/hole/trap occupancy)	n, p, n_t	cm^{-3}	-
Fermi level	E_F	eV	0.3
Excitation fluence	P_{exc}	cm^{-3}	var
Absorbance coefficient at laser wavelength	α	cm	6419281
Diffusion coefficient	$D_{n/p}$	cm^2s^{-1}	-
Electron/hole mobility	$\mu_{n/p}$	$\text{cm}^2\text{V}^{-1}\text{s}^{-1}$	1, 1
Auger recombination coefficient	$k_{aug,n/p}$	cm^6s^{-1}	1×10^{-28}
External radiative band-to-band recombination coefficient	$k_{rad,ext}$	cm^3s^{-1}	5×10^{-12}
Conduction band/valence band energy	E_{CB}, E_{VB}	eV	0, 1.25
Conduction band/valence band density of states	N_C, N_V	cm^{-3}	6.98×10^{18} , 2.49×10^{18}

Effective mass of electron/hole	m_e, m_h	-	0.2, 0.2
Electron/hole capture coefficient	$\beta_{n/p}$	cm^3s^{-1}	var
Trap energy	E_T	eV	var
Trap density	N_t	cm^{-3}	var

$$n_0 = 2 \left(\frac{m_n kT}{2\pi\hbar^2} \right)^{\frac{3}{2}} e^{-\frac{(E_{CB} - E_F)}{kT}} \quad p_0 = 2 \left(\frac{m_p kT}{2\pi\hbar^2} \right)^{\frac{3}{2}} e^{-\frac{(E_F - E_{VB})}{kT}} \quad (6)$$

$$n = n_0 + \Delta n, \quad p = p_0 + \Delta p \quad (7)$$

$$G(x) = P_{exc} \cdot e^{-\alpha x} \quad (8)$$

$$D_{n/p} \frac{d^2 n/p}{dx_i^2} = \frac{\mu_p kT}{e} \frac{\frac{n_{i-1} - n_i}{x_i - x_{i-1}} - \frac{n_i - n_{i+1}}{x_{i+1} - x_i}}{\frac{(x_{i+1} - x_{i-1})}{2}} \quad (9)$$

$$R_{aug} = (k_{aug,n}n + k_{aug,p}p) (np - n_0p_0) \quad (10)$$

$$R_{rad} = k_{rad,ext}(np - n_0p_0) \quad (11)$$

$$R_{trap1,n} = \beta_n n (N_t - n_t) - \beta_n \left(N_C e^{\frac{E_T - E_{CB}}{kT}} \right) n_t \quad (12)$$

$$R_{trap1,p} = \beta_p p n_t - \beta_p \left(N_V e^{\frac{E_{VB} - E_T}{kT}} \right) (N_t - n_t) \quad (13)$$

To simulate TRPL, the system of ODEs (3-5) was solved using the LSODA solver with initial carrier densities n_0 , p_0 and all traps fully unpopulated. If some carrier densities were found to not decay to their original values by the end of the TRPL measurement window (10 ms), the ODEs were solved again with the new initial carrier condition given by the carrier densities at the end of the decay. The TRPL decay was simulated with the obtained electron and hole densities (equation 14).

$$TRPL(t) = \sum k_{rad,ext} n(x,t) p(x,t) \quad (14)$$

To simulate PLQE, the simultaneous system of equations 15 was solved for steady-state carrier densities $n(x)$ and $p(x)$. The trap-assisted non-radiative recombination rate and external PLQE were then calculated as in equations 17, 18.

$$\frac{dn}{dt}(x, t) = 0 \quad n - n_0 + n_{trapped} = p - p_0 + p_{trapped} \quad (15)$$

$$R_{SRH} = \frac{N_t \beta_n \beta_p (np - n_0 p_0)}{(n + N_c e^{\frac{E_T - E_{CB}}{kT}}) \beta_n + (p + N_v e^{\frac{E_{CB} - E_T}{kT}}) \beta_p} \quad (17)$$

$$PLQE = \frac{\sum R_{rad}(x)}{\sum R_{aug}(x) + R_{rad}(x) + R_{SRH}(x)} \quad (18)$$

TRPL and PLQE measurements of control films were replicated with a single electron trap with an energy level 0.3 eV from the CB, a density of $1.6 \times 10^{15} \text{ cm}^{-3}$, and symmetrical electron and hole capture coefficients of $10^{-9} \text{ cm}^3 \text{ s}^{-1}$.

Inductively Coupled Plasma Mass Spectrometry

Inductively coupled plasma mass spectrometry (ICP-MS) was carried out by two different labs, to enable measurement of all samples.

For FAI, CsI and PbI₂:

Concentration of impurities (Sb and Bi) in precursors was determined via triple-quadrupole inductively coupled plasma mass spectrometry (QqQ-ICP-MS). Briefly, FAI and CsI samples were dissolved in 3% HNO₃ (semiconductor grade). PbI₂ samples were dissolved in 3% HNO₃ (semiconductor grade), sonicated and then centrifuged and filtered (0.45 μm syringe filter; Infocroma AG, Goldau, Switzerland). Triplicates were used for each precursor. ¹¹⁵In⁺, ¹²¹Sb⁺ and ²⁰⁹Bi⁺ were measured via 8800 QqQ-ICP-MS (Agilent, Basel, Switzerland) using general-purpose operational settings and helium as a collision gas (5 mL/min). Quantification was performed by external calibration from multi-element standard prepared in 3%

HNO₃ from 0-50 µg/L and was considered appropriate if R²>0.995. ¹⁰³Rh⁺ was monitored as an internal standard to account for possible matrix effects. The concentration of the analytes was further verified by external standard addition.

For SnI₂ A, SnI₂ B, Sn, SnF₂:

The concentration of impurities (Sb and Bi) in precursors was determined via inductively coupled plasma mass spectrometry (ICP-MS, Perkin Elmer NexION 2000). SnI₂ A, SnI₂ B, SnF₂, and Sn samples were dissolved in 2% HNO₃. Digestion was performed according to the parameters outlined in the table below. As some solids persisted in the samples, digestion was performed again, after which any remaining solids (deemed insoluble in HNO₃) were filtered out. Triplicates were used for each precursor.

	T (°C)	p (bar)	Ramp	Hold	Power (%)
1	160	30	5	5	50
2	190	30	3	45	40
3	50	30	1	15	0

¹²¹Sb⁺ and ²⁰⁹Bi⁺ were measured via Perkin Elmer NexION 2000 using helium as a collision gas. Quantification was performed by external calibration from multi-element standard prepared in 2% HNO₃ from 10-200 ppb and was considered appropriate if R²> 0.995. A 2% HNO₃ blank sample was periodically analyzed, and no carry over was detected in these blanks. The blank raw intensities (0.000 ppm for Sb and 0.008 ppm for Bi) fell below the intensity of the lowest calibration point. Data which fell below the raw intensities of the lowest calibration point (10ppb) was discounted and displayed as “not detected”.

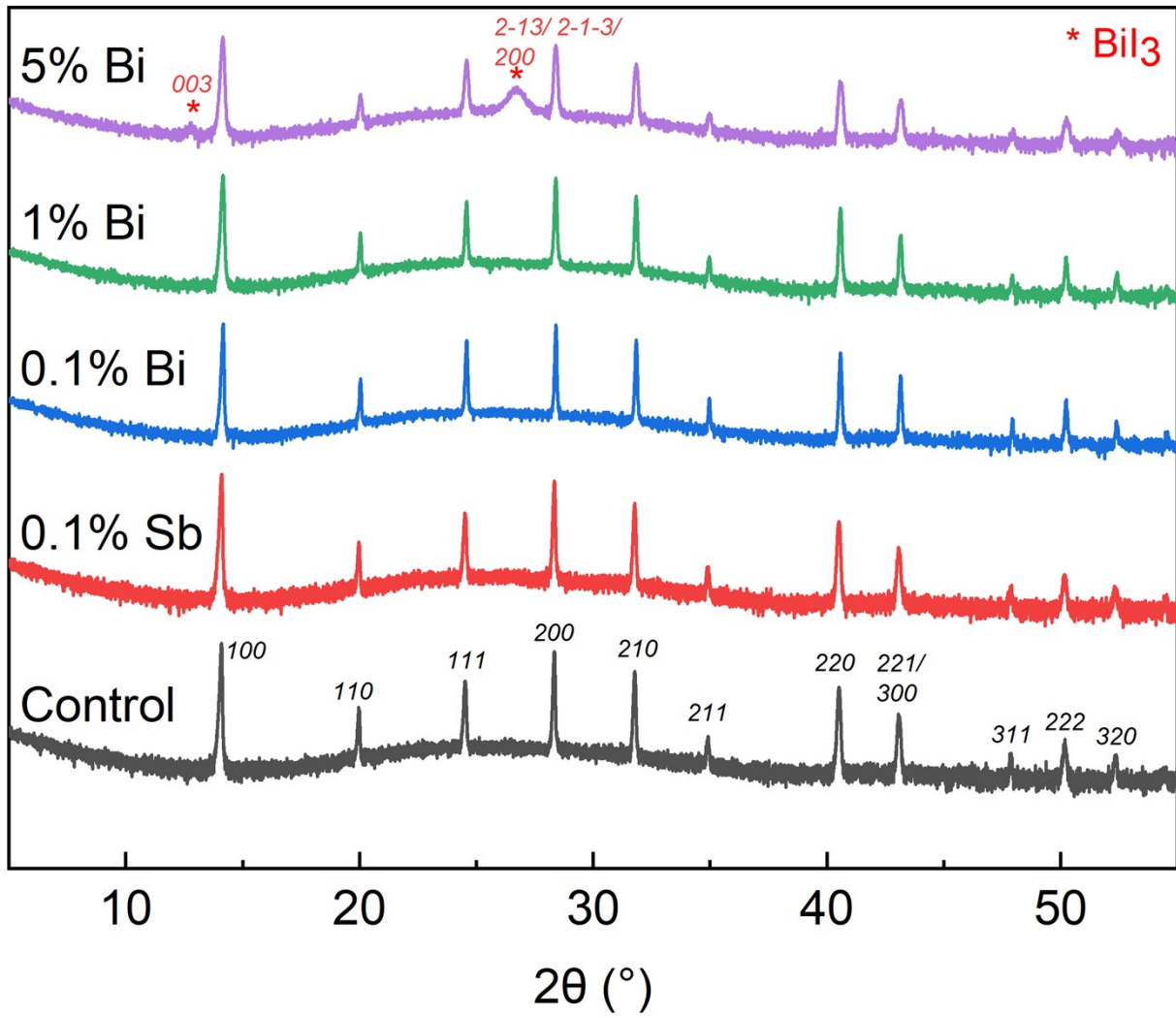


Figure S1. X-ray diffraction (XRD) measurements of $\text{FA}_{0.83}\text{Cs}_{0.17}\text{Pb}_{0.5}\text{Sn}_{0.5}\text{I}_3$ films doped with various concentrations of Bi^{3+} and Sb^{3+} , with intensity scaled on a log scale.

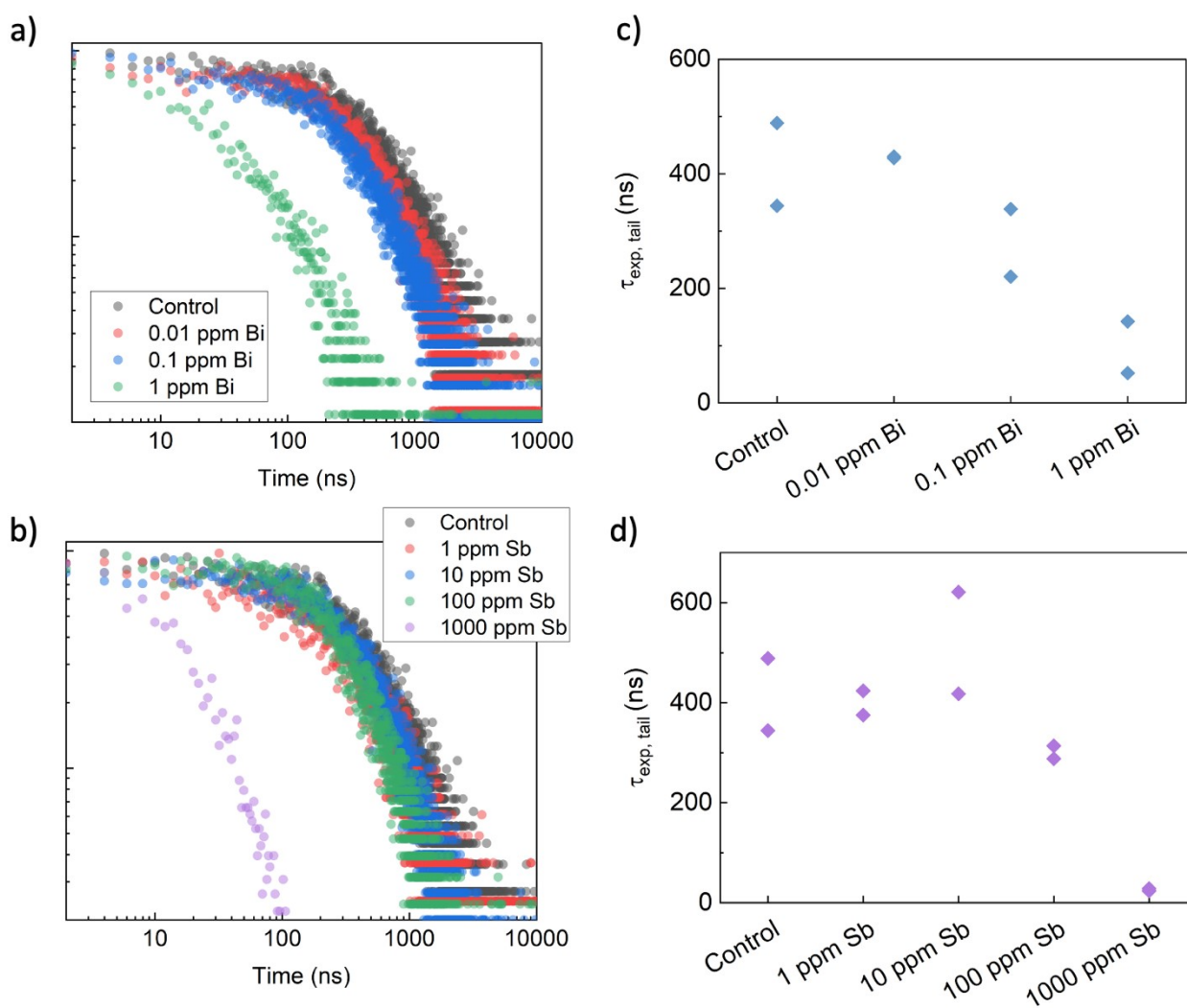


Figure S2. a), b) Normalized time-resolved photoluminescence decays of lead-tin perovskite films doped with small quantities of Bi³⁺ and Sb³⁺. Decays were measured with a repetition rate of 10 kHz and using a 630 nm with an excitation density of 3.1 nJ cm⁻² pulse⁻¹ and a spot size of 2.4 x 10⁻³ cm². c), d) Photoluminescence lifetimes resulting from monoexponential fits to the decays presented in a) and b). Fits were performed from 200 ns until the point in the decay where the signal-to-noise ratio fell below 2. For decays with lifetimes shorter than 200 ns, fits were performed on the 50 ns before the point in the decay where the signal-to-noise ratio fell below 2.

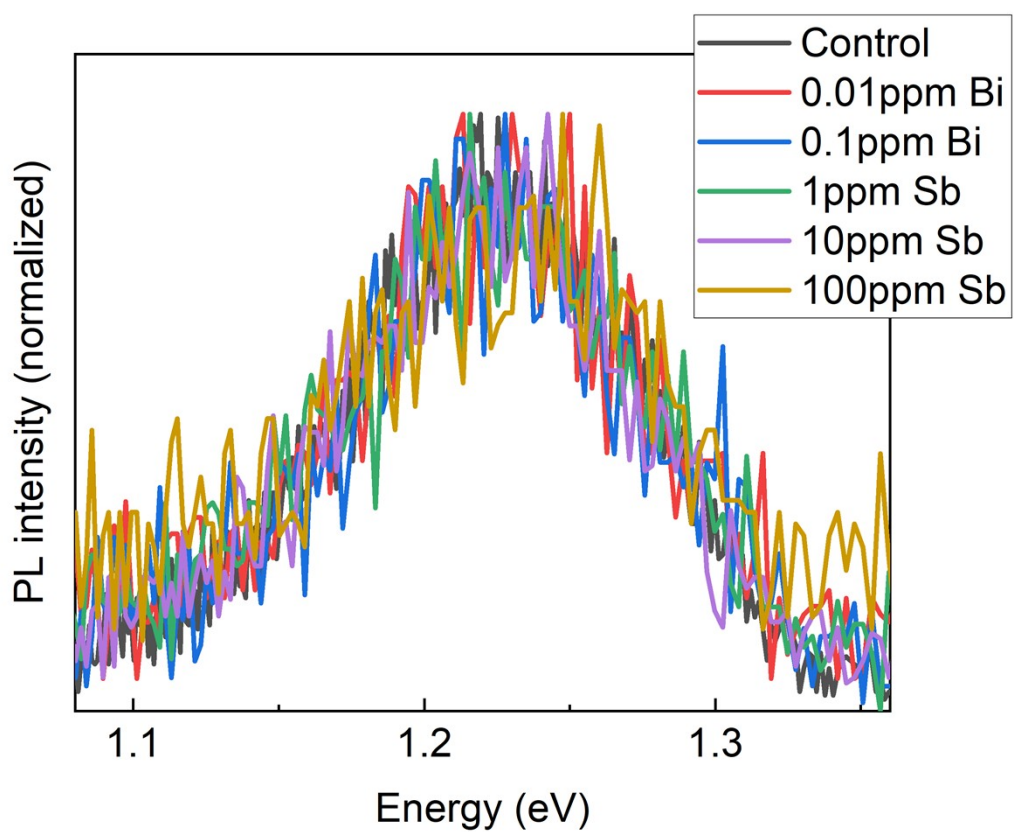


Figure S3. Steady-state photoluminescence peaks of lead-tin perovskite films doped with various densities of BiI₃ or SbI₃, measured during excitation with a 630 nm laser.

Table S1. Defect formation energies (DFE) in eV of Bi dopant in different positions of the $\text{MAPb}_{0.5}\text{Sn}_{0.5}\text{I}_3$ lattice: interstitial position (Bi_i^{3+}), substitutional to the MA cation ($\text{Bi}_{\text{MA}}^{2+}$) and substitutional to the Pb / Sn metal ($\text{Bi}_{\text{Pb}}^+ / \text{Bi}_{\text{Sn}}^+$). DFEs have been calculated at the PBE-D3 level of theory at the VBM of the perovskite.

Defect	I-medium
Bi_i^{3+}	1.74
$\text{Bi}_{\text{MA}}^{2+}$	1.01
Bi_{Pb}^+	-0.03
Bi_{Sn}^+	0.11
Sb_{Pb}^+	-0.03
Sb_{Sn}^+	0.12

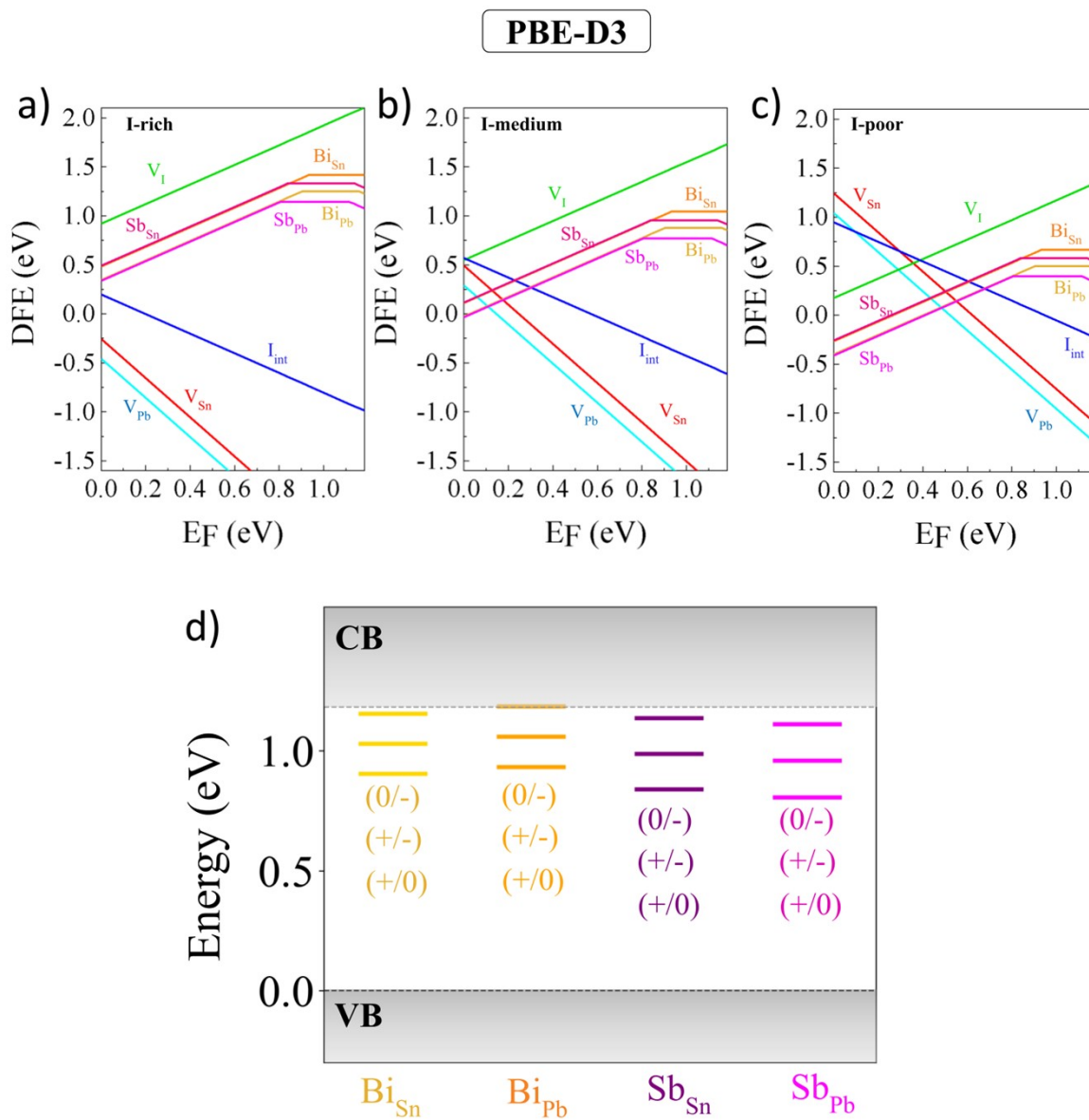


Figure S4. a-c) Defect formation energies of substitutional Bi and Sb dopants in different conditions of growth of the $\text{MAPb}_{0.5}\text{Sn}_{0.5}\text{I}_3$ perovskite; b) associated thermodynamic ionization levels. Defect properties are calculated at the PBE-D3 level of theory.

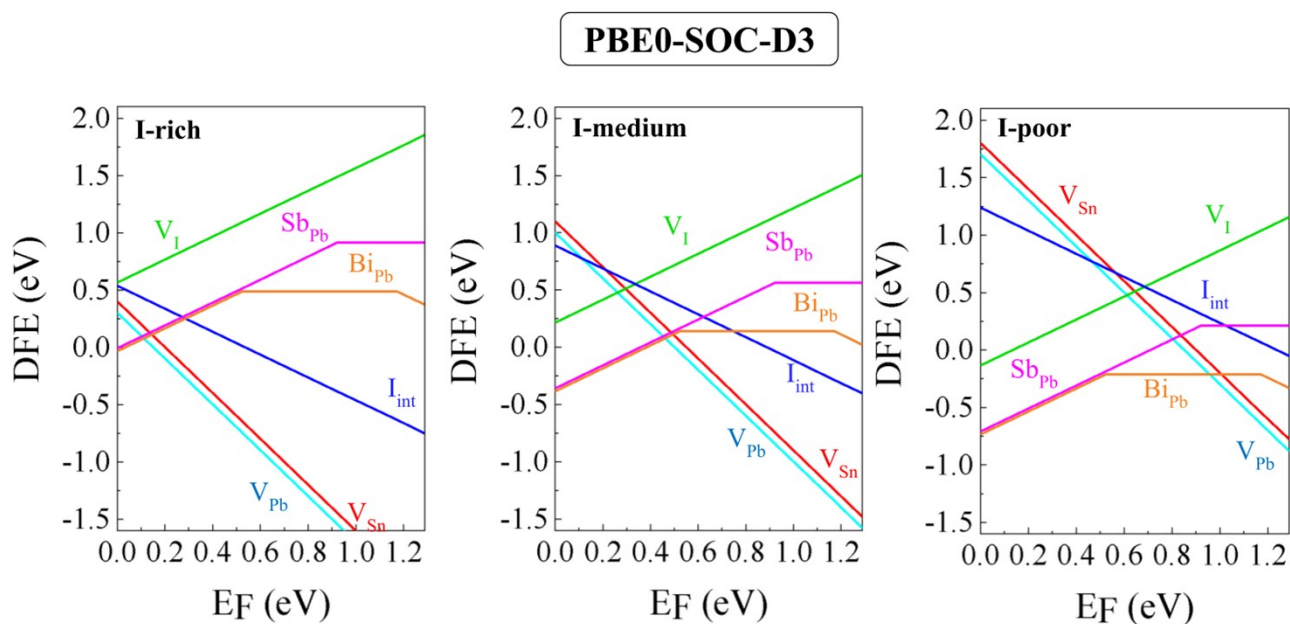


Figure S5. Defect formation energies of Bi and Sb dopants in substitutional positions to Pb in different conditions of growth of the $MAPb_{0.5}Sn_{0.5}I_3$ perovskites, as calculated at the PBE0-SOC-D3 ($\alpha=0.20$) level of theory.

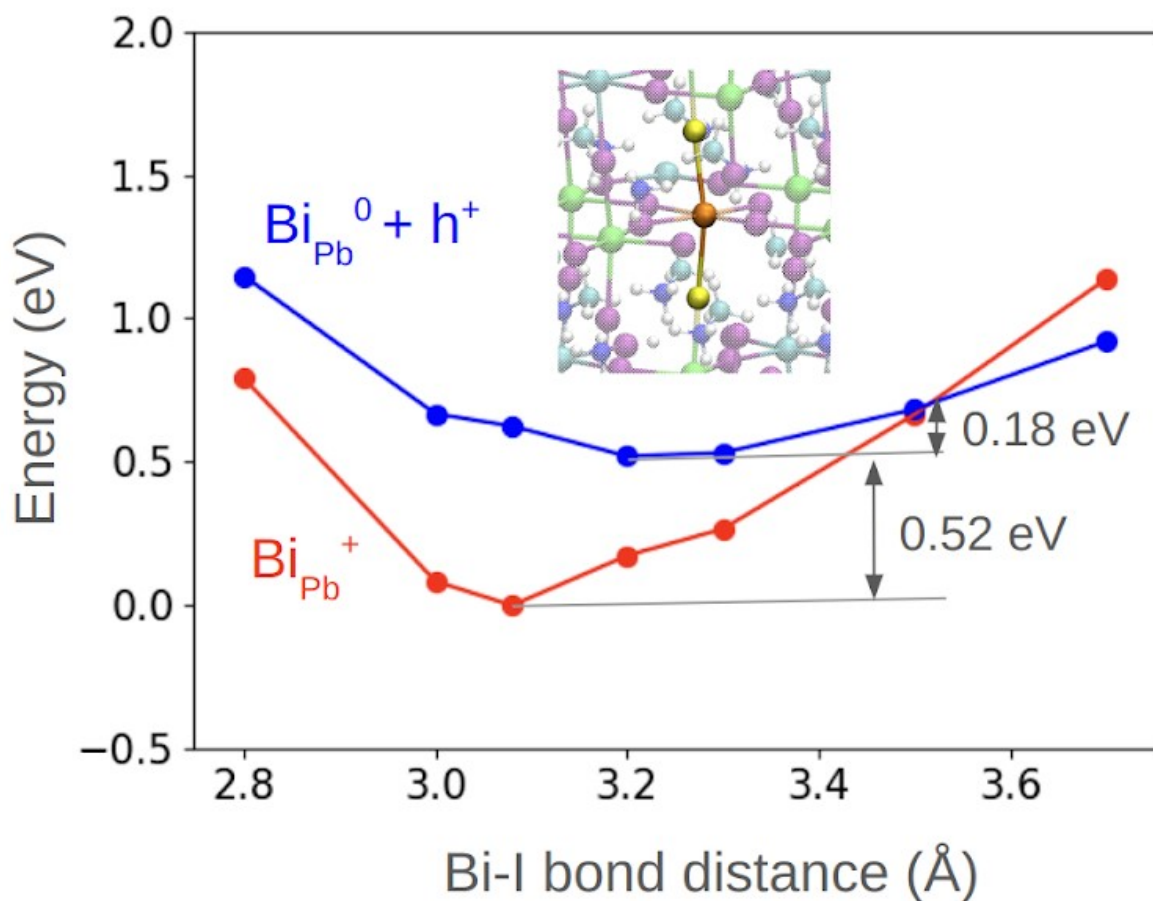


Figure S6. Energy-coordinate diagram for the non-radiative recombination of the hole on the Bi_{Pb}^0 dopant site. The monitored coordinate is the bond distance between the Bi dopant and two apical I, reported in orange and yellow in the inset, respectively. The difference in energy between the minimum of the positive and the neutral state, i.e. the (+/0) transition, is that calculated at the PBE0-SOC-D3 level (0.52 eV), while distortions along the Bi-I bond are calculated at the PBE-D3 level. A barrier to recombination of 0.18 eV is estimated.

Table S2. Descriptions of commercially available perovskite precursor chemicals tested by ICP-MS.

It should be noted that samples were taken from containers which had been in use for some time, in a glovebox area where salts of Bi and Sb were also occasionally handled. Hence this data is not necessarily representative of a certain batch or supplier of material.

Chemical	Description & purity, if provided	Supplier
FAI	>99.99%	Greatcellsolar
CsI	99.9%	Alfa Aesar
PbI ₂	Beads, ultra dry, 99.999% (metals basis)	Thermo Fisher Scientific
SnI ₂ A	Beads, ultra dry, 99.999% (metals basis)	Thermo Fisher Scientific
SnI ₂ B	Powder, for perovskite precursor, >97.0%	TCI
SnF ₂	99.9%	Sigma Aldrich
Sn(0)	99.5%	Sigma Aldrich

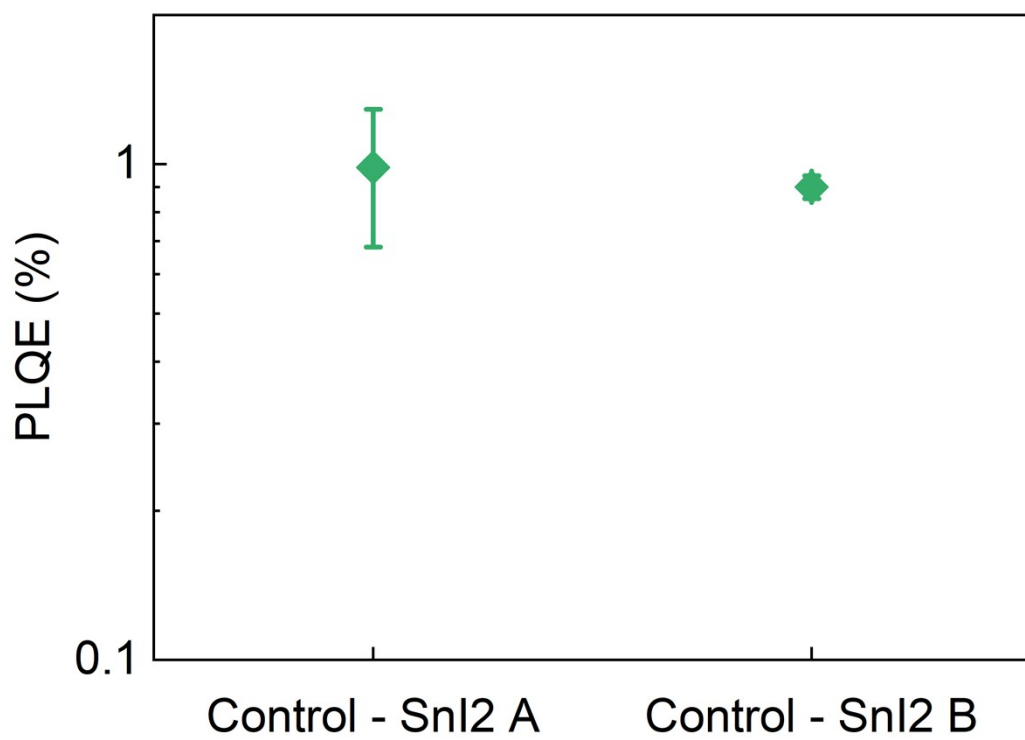


Figure S7. PLQE of lead-tin perovskite films fabricated either with SnI₂ from supplier A, which was determined by ICP-MS to contain <0.01 ppm Bi, or with SnI₂ from supplier B, which was determined by ICP-MS to contain 1 ppm Bi.

References

- (1) de Mello, J. C.; Wittmann, H. F.; Friend, R. H. An Improved Experimental Determination of External Photoluminescence Quantum Efficiency. *Adv. Mater.* **1997**, *9* (3), 230–232. <https://doi.org/10.1002/adma.19970090308>.
- (2) Zeiske, S.; Kaiser, C.; Meredith, P.; Armin, A. Sensitivity of Sub-Bandgap External Quantum Efficiency Measurements of Solar Cells under Electrical and Light Bias. *ACS Photonics* **2020**, *7* (1), 256–264. <https://doi.org/10.1021/acsp Photonics.9b01531>.
- (3) Giannozzi, P.; Baroni, S.; Bonini, N.; Calandra, M.; Car, R.; Cavazzoni, C.; Ceresoli, D.; Chiarotti, G. L.; Cococcioni, M.; Dabo, I.; Dal Corso, A.; De Gironcoli, S.; Fabris, S.; Fratesi, G.; Gebauer, R.; Gerstmann, U.; Gougoussis, C.; Kokalj, A.; Lazzeri, M.; Martin-Samos, L.; Marzari, N.; Mauri, F.; Mazzarello, R.; Paolini, S.; Pasquarello, A.; Paulatto, L.; Sbraccia, C.; Scandolo, S.; Sclauzero, G.; Seitsonen, A. P.; Smogunov, A.; Umari, P.; Wentzcovitch, R. M. QUANTUM ESPRESSO: A Modular and Open-Source Software Project for Quantum Simulations of Materials. *J. Phys. Condens. Matter* **2009**, *21* (39), 395502. <https://doi.org/10.1088/0953-8984/21/39/395502>.
- (4) Grimme, S.; Antony, J.; Ehrlich, S.; Krieg, H. A Consistent and Accurate *Ab Initio* Parametrization of Density Functional Dispersion Correction (DFT-D) for the 94 Elements H-Pu. *J. Chem. Phys.* **2010**, *132* (15), 154104. <https://doi.org/10.1063/1.3382344>.
- (5) Stoumpos, C. C.; Malliakas, C. D.; Kanatzidis, M. G. Semiconducting Tin and Lead Iodide Perovskites with Organic Cations: Phase Transitions, High Mobilities, and Near-Infrared Photoluminescent Properties. *Inorg. Chem.* **2013**, *52* (15), 9019–9038. <https://doi.org/10.1021/ic401215x>.
- (6) Hamann, D. R.; Schlüter, M.; Chiang, C. Norm-Conserving Pseudopotentials. *Phys. Rev. Lett.* **1979**, *43* (20), 1494–1497. <https://doi.org/10.1103/PhysRevLett.43.1494>.
- (7) Van Setten, M. J.; Giantomassi, M.; Bousquet, E.; Verstraete, M. J.; Hamann, D. R.; Gonze, X.; Rignanese, G.-M. The PseudoDojo: Training and Grading a 85 Element Optimized Norm-Conserving Pseudopotential Table. *Comput. Phys. Commun.* **2018**, *226*, 39–54. <https://doi.org/10.1016/j.cpc.2018.01.012>.
- (8) Van De Walle, C. G.; Neugebauer, J. First-Principles Calculations for Defects and Impurities: Applications to III-Nitrides. *J. Appl. Phys.* **2004**, *95* (8), 3851–3879. <https://doi.org/10.1063/1.1682673>.
- (9) Adamo, C.; Barone, V. Toward Reliable Density Functional Methods without Adjustable Parameters: The PBE0 Model. *J. Chem. Phys.* **1999**, *110* (13), 6158–6170. <https://doi.org/10.1063/1.478522>.
- (10) Perdew, J. P.; Ernzerhof, M.; Burke, K. Rationale for Mixing Exact Exchange with Density Functional Approximations. *J. Chem. Phys.* **1996**, *105* (22), 9982–9985. <https://doi.org/10.1063/1.472933>.
- (11) Gražulis, S.; Chateigner, D.; Downs, R. T.; Yokochi, A. F. T.; Quirós, M.; Lutterotti, L.; Manakova, E.; Butkus, J.; Moeck, P.; Le Bail, A. Crystallography Open Database – an Open-Access Collection of Crystal Structures. *J. Appl. Crystallogr* **2009**, *42* (4), 726–729.